Signal Processing 92 (2012) 2519–2524

Contents lists available at SciVerse ScienceDirect

Signal Processing

journal homepage: www.elsevier.com/locate/sigpro

Near-field scattering centers estimation using a far-field 3-D ESPRIT type method

Shiyong Li [a,*], Houjun Sun [a], Xin Lv [a], Bocheng Zhu [b]

[a] School of Information and Electronics, Beijing Institute of Technology, Beijing 100081, China
[b] Institute of Electronic Engineering, Peking University, Beijing 100871, China

ARTICLE INFO

Article history:
Received 14 July 2011
Received in revised form
26 January 2012
Accepted 25 March 2012
Available online 2 April 2012

Keywords:
Scattering centers
Near-field
Far-field
ESPRIT

ABSTRACT

A method is presented for estimating the three-dimensional (3-D) scattering centers of an object under spherical wave illumination. A novel approximation of the distance from the antenna to each scattering center is first formulated, which provides an approach for compensating for the spherical wavefront curvature. Additionally, the approximation transforms the near-field problem into virtual far-field problem. A far-field 3-D ESPRIT type algorithm is also presented and applied to estimating the virtual far-field scattering centers. Finally, the near-field scattering centers are obtained by using the compensation relations. Simulation results show the performance improvement of the proposed method compared with the conventional far-field method.

© 2012 Elsevier B.V. All rights reserved.

1. Introduction

In radar applications, an electrically large object can often be conceptually resolved into collections of scattering centers which correspond to the points radiating high-energy radar cross section (RCS) [1,2]. Radar images present a spatial distribution of scattering centers. The scattering center concept provides a concise and physical description for scattering mechanisms of an object, and therefore it has been extensively used in numerous radar applications [3], such as synthetic aperture radar (SAR) or inverse SAR (ISAR) target feature extraction [4], automatic target recognition (ATR) [5,6], and electromagnetic signature data compression [7]. Extracting the scattering center parameters from wideband radar measurements is one of the concerns in high-resolution radar signal processing [8]. Conventionally, Fourier technique is an easily implemented approach and computationally efficient, however the resolution is restricted by Rayleigh limit [9].

Model-based algorithms can overcome the limitation and provide higher resolutions than the Fourier-based techniques. These algorithms include, for example, multiple signal classification (MUSIC) [10,11], estimation of signal parameters via rotational invariance techniques (ESPRIT) [12,13], matrix enhancement and matrix pencil (MEMP) [14], and maximum likelihood (ML) [15]. The aforementioned methods assume that the objects of interest are located relatively far from the antenna so that the wavefronts to them can be regarded as plane waves. However, this assumption is no longer valid for higher frequencies or larger objects, and the waves illuminating the object zone must be considered as spherical waves. Since the available methods based on the far-field assumption cannot be directly applied to the near-field scenario, near-field imaging or sources localization is typically solved by other means, such as the modified versions of ML and 2-D MUSIC [16], and higher-order statistics [17]. The near-field methods need exhaustive multidimensional search or higher-order statistics, both of which are computationally inefficient.

In this paper, we first propose a novel approximation of the distance from the antenna to each scattering center

* Corresponding author. Tel.: +86 13520549802.
E-mail address: lisy_0723@hotmail.com (S. Li).

0165-1684/$ - see front matter © 2012 Elsevier B.V. All rights reserved.
10.1016/j.sigpro.2012.03.016

in Section 2. The approximation provides an approach for compensating for the spherical wavefront curvature and additionally transforms the near-field problem into virtual far-field problem. Also, it is compared with the Fresnel approximation [18,19], which is also known as the second-order Taylor approximation [20]. In Section 3, based on the MEMP method [14] and the 2-D ESPRIT type method [21], we present a 3-D ESPRIT type algorithm. The virtual far-field scattering centers are first estimated by the 3-D ESPRIT type algorithm, and then they are transformed into the real ones by applying the near-field compensation relations. The results demonstrating the accuracy of near-field compensation are shown in Section 4. Section 5 summarizes the conclusions.

2. Near-field compensation

The setup for 3-D imaging is shown in Fig. 1 in which an object formed by a distribution of isotropic point scattering centers of reflectivity $g(x,y,z)$ is rotated about the z-axis. The radar antenna is located at a distance R_0 from the rotation center. Thus, the Born-approximated (made by almost all work on radar imaging [22]) backscattered (also calibrated) electric fields (horizontal or vertical component) are given by

$$y_s(k,\varphi,\theta) = \int_x\int_y\int_z [g(x,y,z)/\sigma_0] \times \frac{R_0^2 \exp\{-j2\pi k[R_{\varphi,\theta}(x,y,z)-R_0]\}}{R_{\varphi,\theta}^2(x,y,z)} \mathrm{d}x\mathrm{d}y\mathrm{d}z, \quad (1)$$

where $k=2f/c$, f is the operating frequency, c is the speed of light, and σ_0 is the RCS of the calibrator located at the rotation center. $R_{\varphi,\theta}(x,y,z)$ is the distance from the antenna to each scattering center such as

$$R_{\varphi,\theta}(x,y,z) = \sqrt{R_0{}^2+x^2+y^2+z^2+2R_0[(-x\sin\varphi+y\cos\varphi)\sin\theta-z\cos\theta]}, \quad (2)$$

where φ is the azimuth position of the rotating platform, and θ is the looking angle of the radar antenna as shown in Fig. 1.

From (1) and (2), we can see that the propagation delay is not linearly varying with the locations of scattering centers or the angular variables, and the far-field based estimation methods are no longer applicable. If the antenna is located in the far-field zone of the object, Eq. (2) reduces to an often used form:

$$R_F \approx R_0 + (-x\sin\varphi + y\cos\varphi)\sin\theta - z\cos\theta. \quad (3)$$

For the near-field case, instead of using the Fresnel approximation, we approximate (2) by first extracting (3) from the square root and then expanding the remainder in a power series and keeping only the lower order terms. Further, the higher-order infinitesimals of the trigonometric functions are ignored. Then we get

$$R_{\varphi,\theta}(x,y,z) \approx R_0 - x\sin\varphi + y\cos\varphi - z\cos\theta + (x^2\cos\varphi + z^2\sin\theta + 2xy\sin\varphi + 2yz\cos\theta)/[2(R_0+y)]. \quad (4)$$

Under further assumption of small angular variation [23], (4) can be approximately written as

$$R_{\varphi,\theta}(x,y,z) \approx R_0 + x'\varphi' + y' + z'\theta', \quad (5)$$

where $\varphi'=\varphi$, $\theta'=\pi/2-\theta$, $x'=-x+xy/(R_0+y)$, $y'=y+x^2/[2(R_0+y)]+z^2/[2(R_0+y)]$, and $z'=-z+yz/(R_0+y)$. And therefore

$$y = R_0(2R_0y' - x'^2 - z'^2)/(2R_0^2 + x'^2 + z'^2) \quad (6)$$

$$x = -x'(R_0+y)/R_0, \quad (7)$$

$$z = -z'(R_0+y)/R_0. \quad (8)$$

When the angle range is large, we choose to use the model in (4), since it is more accurate than (5). In this case, "resampling" is needed to cast the data into the equally spaced format in the Cartesian coordinates.

The restriction on the minimum measuring distance R_0 is also considered. If we use $\lambda/16$ as the maximum error between (4) and (2) at $\varphi'=0$ and $\theta=\pi/2$, we obtain

$$R_0 \geq [D^4/(2\lambda)]^{1/3} + D/2, \quad (9)$$

where D is the side length of the a cubic image zone, and λ is the wavelength of the operating signal. Clearly, the right part of (9) is smaller than the Fresnel near-field

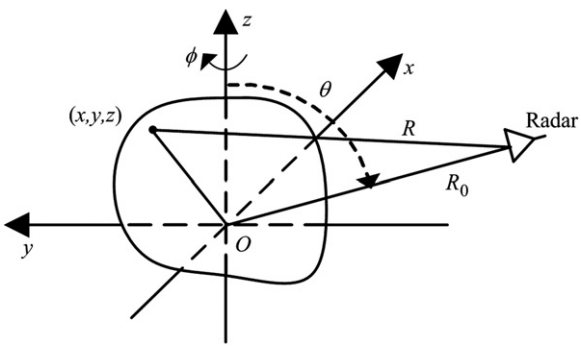

Fig. 1. Geometrical parameters of the measurement and imaging situation.

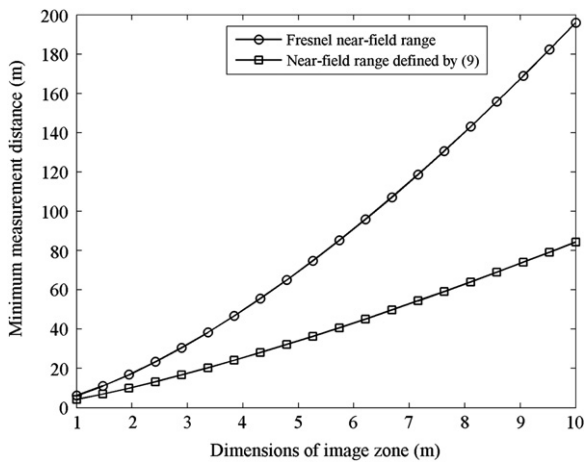

Fig. 2. Comparison of the minimum measurement distances defined by (9) and the Fresnel approximation, respectively. Assuming the maximum error is $\lambda/16$, and $\lambda=0.01$ m.

region $0.62\sqrt{D^3/\lambda}$ [18], as shown in Fig. 2, i.e., (9) can be applied to nearer measurement distance.

Next, we introduce the Fresnel approximation for comparison:

$$R_{\varphi,\theta}(x,y,z) \approx R_0 - x\sin\varphi + y\cos\varphi - z\cos\theta + (x^2\cos\varphi + z^2\sin\theta + 2xy\sin\varphi + 2yz\cos\theta)/(2R_0). \quad (10)$$

Similarly, this equation is under the assumption of small angular variation. It is also known as the second-order Taylor series approximation, and has been found in many references on near-field source localization [24,25], and electromagnetic scattering computation [19].

Considering a cubic image zone, we compare the approximation errors of (4) and (10) for the two side planes at $y=-D/2$ and $z=D/2$, respectively, at $\varphi=0$ and $\theta=\pi/2$ for the sake of simplicity (errors for the side plane at $x=D/2$ are the same as the side plane at $z=D/2$). For this special case, the exact distance (2) can be given by

$$R_{0,\pi/2}(x,y,z) = \sqrt{(R_0+y)^2+x^2+z^2} = \sqrt{(R_0+y)^2+x'^2} = (R_0+y)\sqrt{1+\frac{x'^2}{(R_0+y)^2}} \quad (11)$$

where $x'^2 = x^2+z^2$. And (4) or (5) becomes

$$R_{0,\pi/2}(x,y,z) \approx R_0 + y + \frac{x^2+z^2}{2(R_0+y)} = (R_0+y) + \frac{x'^2}{2(R_0+y)} \quad (12)$$

The Fresnel approximation (10) becomes

$$R_{0,\pi/2}(x,y,z) \approx R_0 + y + \frac{x^2+z^2}{2R_0} = (R_0+y) + \frac{x'^2}{2R_0} \quad (13)$$

It can be seen from (11) to (13), the difference between the two approximations is that (12) is the second-order Taylor series approximation to $R_{0,\pi/2}(x,y,z)$ about point $(0,y,0)$ (assuming that y is constant), and (13) is the second-order Taylor series approximation to $R_{0,\pi/2}(x,y,z)$ about point (0,0,0). In the x–z section planes (with y equals constant), the approximation (12) is apparently more accurate than (13). The numerical comparison is shown in Fig. 3(a). However, for the x–y or y–z section planes, the approximation errors are hard to estimate. We only give the numerical results of the approximation errors as shown in Fig. 3(b). Clearly, the errors of (12) or (4) are smaller than the errors of (13) or (10) for the major part of the section planes, except near the neighborhood of $y=0$ (within the $y<0$ part) for the x–y plane.

The denominator in (1) is considerably less sensitive than its exponent to approximations for $R_{\varphi,\theta}(x,y,z)$. Accordingly, a further approximation is given by:

$$R_{\varphi,\theta}^2/R_0^2 \approx 1 + (x^2+y^2+z^2)/R_0^2 + 2y/R_0 \quad (14)$$

Using (5) and (14) in (1), we obtain

$$y_s(k,\varphi,\theta) = \int_x\int_y\int_z g'(x,y,z)\exp[-j2\pi k(x'\varphi'+y'+z'\theta')]\mathrm{d}x\mathrm{d}y\mathrm{d}z, \quad (15)$$

where

$$g'(x,y,z) = \frac{g(x,y,z)/\sigma_0}{1+(x^2+y^2+z^2)/R_0^2+2y/R_0}.$$

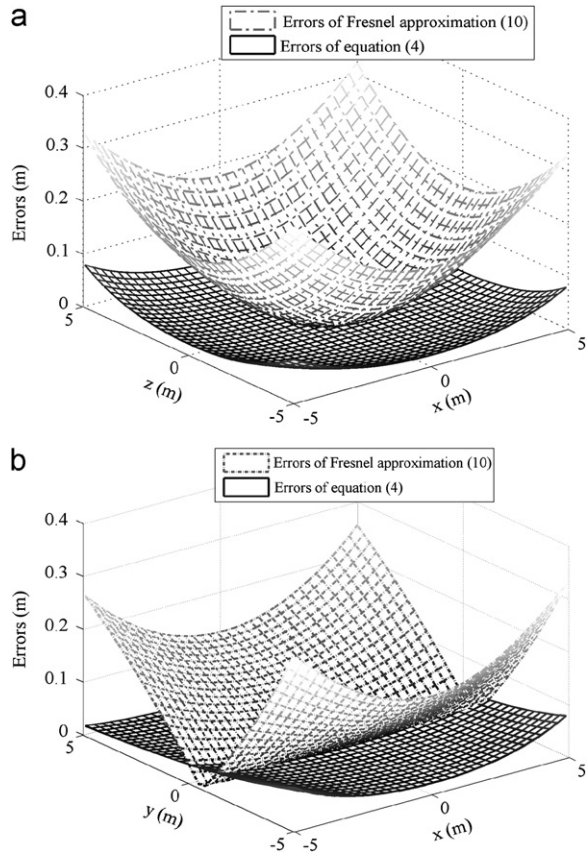

Fig. 3. Errors of the approximations, where the real line meshes represent the errors of (4), and the "–." meshes represent the errors of Fresnel approximation (10) both at $\varphi'=0$, $\theta=\pi/2$, and $R_0=20$ m. (a) errors for x–z plane at $y=-D/2$, (b) errors for x–y plane at $z=D/2$.

Note that (15) represents a far-field problem and it can be discretized as follows:

$$y_s(n,m,i) = \sum_{l=0}^{L-1} a_l p_{1l}^n p_{2l}^m p_{3l}^i,$$
$$n=0,1,\ldots,N-1;\quad m=0,1,\ldots,M-1;\quad i=0,1,\ldots,I-1. \quad (16)$$

where $a_l = g'(x_l,y_l,z_l)\Delta x\Delta y\Delta z\exp(-j2\pi k_0 y_l')$, $p_{1l}=\exp(-j2\pi y_l'\Delta k)$, $p_{2l}=\exp(-j2\pi k_0 x_l'\Delta\varphi')$, and $p_{3l}=\exp(-j2\pi k_0 z_l'\Delta\theta')$. L represents the number of scattering centers. Eq. (16) is in the form of a sum-of-exponential model, with linear phase dependence with respect to Δk, $\Delta\varphi'$, and $\Delta\varphi'$, respectively. Obviously, any far-field based 3-D estimation algorithm can be used to estimate the unknown parameters in (16). After estimating the virtual far-field scattering centers, the second step is to transform the virtual ones into the real ones by using the relations (6) to (8).

3. 3-D ESPRIT type algorithm

The original data matrix will be ill-conditioned when its rank is less than the number of scattering centers, i.e., L in (16). Thus an enhanced matrix is formed from the original data to solve the ill-conditioned problem [14]. It is defined as

follows:

$$\mathbf{Y}_e = \begin{bmatrix} \mathbf{Y}_0 & \mathbf{Y}_1 & \cdots & \mathbf{Y}_{N-Q} \\ \mathbf{Y}_1 & \mathbf{Y}_2 & \cdots & \mathbf{Y}_{N-Q+1} \\ \vdots & \vdots & & \vdots \\ \mathbf{Y}_{Q-1} & \mathbf{Y}_Q & \cdots & \mathbf{Y}_{N-1} \end{bmatrix}, \tag{17}$$

where

$$\mathbf{Y}_n = \begin{bmatrix} \mathbf{Y}(n,\ 0) & \mathbf{Y}(n,\ 1) & \cdots & \mathbf{Y}(n,\ M-P) \\ \mathbf{Y}(n,\ 1) & \mathbf{Y}(n,\ 2) & \cdots & \mathbf{Y}(n,\ M-P+1) \\ \vdots & \vdots & & \vdots \\ \mathbf{Y}(n,\ P-1) & \mathbf{Y}(n,\ P) & \cdots & \mathbf{Y}(n,\ M-1) \end{bmatrix}, \tag{18}$$

and where

$$\mathbf{Y}(n,\ m) = \begin{bmatrix} y_s(n,\ m,\ 0) & y_s(n,\ m,\ 1) & \cdots & y_s(n,\ m,\ I-R) \\ y_s(n,\ m,\ 1) & y_s(n,\ m,\ 2) & \cdots & y_s(n,\ m,\ I-R+1) \\ \vdots & \vdots & & \vdots \\ y_s(n,\ m,\ R-1) & y_s(n,\ m,\ R) & \cdots & y_s(n,\ m,\ I-1) \end{bmatrix}. \tag{19}$$

Clearly, $\mathbf{Y}_e$ is a $Q\times(N-Q+1)$ Hankel block matrix, $\mathbf{Y}_n$ is a $P\times(M-P+1)$ Hankel block matrix, and $\mathbf{Y}(n,m)$ is an $R\times(I-R+1)$ Hankel matrix. The integers P, Q and R are called the moving window lengths in the m, n and i directions, respectively. The selection of the window lengths must be sufficient to guarantee the matrix $\mathbf{Y}_e$ to be of rank L.

Using (16) in (19), $\mathbf{Y}(n,m)$ becomes

$$\mathbf{Y}(n,\ m) = \mathbf{Z}_L\mathbf{A}\mathbf{X}_d{}^m\mathbf{Y}_d{}^n\mathbf{Z}_R{}^T, \tag{20}$$

where $\mathbf{A}$, $\mathbf{X}_d$ and $\mathbf{Y}_d$ are diagonal matrices such as $\mathbf{A} = \underset{1\le l\le L}{\text{diag}}\,(a_l)$, $\mathbf{X}_d = \underset{1\le l\le L}{\text{diag}}\,(p_{1l})$, and $\mathbf{Y}_d = \underset{1\le l\le L}{\text{diag}}\,(p_{2l})$. $\mathbf{Z}_L$ and $\mathbf{Z}_R$ are Vandermonde matrices of size $R\times L$ and $(I-R+1)\times L$ such as $\mathbf{Z}_L = \{p_{3l}^{\ i}\}_{l=1,\ i=0}^{L,\ R-1}$, $\mathbf{Z}_R = \{p_{3l}{}^i\}_{l=1,\ i=0}^{L,\ I-R}$, respectively. The superscript "T" denotes transpose.

Similarly, using (20) in (18), and eventually in (17) yields

$$\mathbf{Y}_e = \mathbf{W}_L\mathbf{A}\mathbf{W}_R^T, \tag{21}$$

where

$$\mathbf{W}_L = \begin{bmatrix} \mathbf{E}_L^T & \mathbf{X}_d\mathbf{E}_L^T & \cdots & \mathbf{X}_d^{Q-1}\mathbf{E}_L^T \end{bmatrix}^T, \tag{22}$$

$$\mathbf{W}_R = \begin{bmatrix} \mathbf{E}_R^T & \mathbf{X}_d\mathbf{E}_R^T & \cdots & \mathbf{X}_d^{N-Q}\mathbf{E}_R^T \end{bmatrix}^T, \tag{23}$$

$$\mathbf{E}_L = \begin{bmatrix} \mathbf{Z}_L^T & \mathbf{Y}_d\mathbf{Z}_L^T & \cdots & \mathbf{Y}_d^{P-1}\mathbf{Z}_L^T \end{bmatrix}^T, \tag{24}$$

$$\mathbf{E}_R = \begin{bmatrix} \mathbf{Z}_R^T & \mathbf{Y}_d\mathbf{Z}_R^T & \cdots & \mathbf{Y}_d^{M-P}\mathbf{Z}_R^T \end{bmatrix}^T. \tag{25}$$

From (22), it clearly follows that

$$\underline{\mathbf{W}_L}\mathbf{X}_d = \overline{\mathbf{W}_L}, \tag{26}$$

where $\underline{\mathbf{W}_L}$ and $\overline{\mathbf{W}_L}$ are, respectively, formed with the first and the last $(Q-1)PR$ rows of $\mathbf{W}_L$. From (26), the least squares solution of $\mathbf{X}_d$ can be obtained.

Using the structures of $\mathbf{W}_L$ and $\mathbf{E}_L$, respectively, we can also extract $\mathbf{Y}_d$ and $\mathbf{Z}_d$ through some permutations. Here, $\mathbf{Z}_d$ is a diagonal matrix such as $\mathbf{Z}_d = \underset{1\le l\le L}{\text{diag}}\,(p_{3l})$. Two permutation matrices $\mathbf{P}_1$ and $\mathbf{P}_2$ are defined such as

$$\mathbf{P}_1 = \sum_{k=1}^{PR}\sum_{l=1}^{Q}\mathbf{P}_{k,l}^{PR\times Q}\otimes\mathbf{P}_{l,k}^{Q\times PR} \text{ and } \mathbf{P}_2 = \sum_{k=1}^{QR}\sum_{l=1}^{P}\mathbf{P}_{k,l}^{QR\times P}\otimes\mathbf{P}_{l,k}^{P\times QR},$$

where the symbol $\otimes$ denotes the Kronecker product, and $\mathbf{P}_{k,l}^{K\times L}$ is an elementary matrix of size $K\times L$ with 1 for the (k,l) element and 0 elsewhere.

Left multiplying $\mathbf{W}_L$ by $\mathbf{P}_1$ yields

$$\mathbf{W}_{LP1} = \mathbf{P}_1\mathbf{W}_L = \begin{bmatrix} \mathbf{E}_{LP1}^T & \mathbf{Y}_d\mathbf{E}_{LP1}^T & \cdots & \mathbf{Y}_d^{P-1}\mathbf{E}_{LP1}^T \end{bmatrix}^T, \tag{27}$$

where $\mathbf{E}_{LP1} = \begin{bmatrix} \mathbf{X}_L^T & \mathbf{Z}_d\mathbf{X}_L^T & \cdots & \mathbf{Z}_d^{R-1}\mathbf{X}_L^T \end{bmatrix}^T$. Clearly from (27), it follows that

$$\underline{\mathbf{W}_{LP1}}\mathbf{Y}_d = \overline{\mathbf{W}_{LP1}}. \tag{28}$$

Similarly, left multiplying $\mathbf{W}_{LP1}$ by $\mathbf{P}_2$ yields

$$\mathbf{W}_{LP2} = \mathbf{P}_2\mathbf{W}_{LP1} = \begin{bmatrix} \mathbf{E}_{LP2}^T & \mathbf{Z}_d\mathbf{E}_{LP2}^T & \cdots & \mathbf{Z}_d^{R-1}\mathbf{E}_{LP2}^T \end{bmatrix}^T, \tag{29}$$

where $\mathbf{E}_{LP2} = \begin{bmatrix} \mathbf{Y}_L^T & \mathbf{X}_d\mathbf{Y}_L^T & \cdots & \mathbf{X}_d^{Q-1}\mathbf{Y}_L^T \end{bmatrix}^T$. Then we have

$$\underline{\mathbf{W}_{LP2}}\mathbf{Z}_d = \overline{\mathbf{W}_{LP2}}. \tag{30}$$

Next, we introduce the singular value decomposition (SVD) to factorize the matrix $\mathbf{Y}_e$ such as

$$\mathbf{Y}_e = \mathbf{U}_s\mathbf{D}_s\mathbf{V}_s^H + \mathbf{U}_n\mathbf{D}_n\mathbf{V}_n^H, \tag{31}$$

where the superscript "H" denotes the conjugate transpose. $\mathbf{U}_s$, $\mathbf{D}_s$ and $\mathbf{V}_s$ correspond to the signal subspace and contain the L principal components. $\mathbf{U}_n$, $\mathbf{D}_n$ and $\mathbf{V}_n$ contain the remaining components related to the noise subspace. The desired rank of noiseless data matrix $\mathbf{Y}_e$ equals to the number L when the following is true [14].

$$\begin{cases} M-L+1 \ge P \ge L \\ N-L+1 \ge Q \ge L \\ I-L+1 \ge R \ge L \end{cases}. \tag{32}$$

From the analyses of (21) and (31), we know the matrices $\mathbf{W}_L$ and $\mathbf{U}_s$ span the same signal subspace if (32) is true. This implies the existence of a nonsingular matrix $\mathbf{T}$ of size $L\times L$ such that

$$\mathbf{U}_s = \mathbf{W}_L\mathbf{T}. \tag{33}$$

A substitution of (33) into (26) and solving for $\mathbf{X}_d$ yields

$$\mathbf{X}_d = \mathbf{T}(\underline{\mathbf{U}_s})^+\overline{\mathbf{U}_s}\mathbf{T}^{-1} = \mathbf{T}\mathbf{F}_1\mathbf{T}^{-1}, \tag{34}$$

where $\underline{\mathbf{U}_s}$ and $\overline{\mathbf{U}_s}$ are, respectively, formed with the first and the last $(Q-1)PR$ rows of $\mathbf{U}_s$. And the superscript "+" denotes the pseudo-inverse. Further using (33) and the permutation relations among $\mathbf{W}_L$, $\mathbf{W}_{LP1}$ and $\mathbf{W}_{LP2}$, we get

$$\mathbf{Y}_d = \mathbf{T}(\underline{\mathbf{P}_1\mathbf{U}_s})^+\overline{\mathbf{P}_1\mathbf{U}_s}\mathbf{T}^{-1} = \mathbf{T}\mathbf{F}_2\mathbf{T}^{-1} \tag{35}$$

$$\mathbf{Z}_d = \mathbf{T}(\underline{\mathbf{P}_2\mathbf{P}_1\mathbf{U}_s})^+\overline{\mathbf{P}_2\mathbf{P}_1\mathbf{U}_s}\mathbf{T}^{-1} = \mathbf{T}\mathbf{F}_3\mathbf{T}^{-1} \tag{36}$$

However, the aforementioned relations cannot be directly used. In fact, the eigenvectors are not uniquely defined when an eigenvalue has a multiplicity greater than 1. To avoid this

case, a linear combination of the matrices can be used to obtain an unique transformation $\mathbf{T}_u$:

$$\mathbf{T}_u(\alpha\mathbf{F}_x+\beta\mathbf{F}_y+\gamma\mathbf{F}_z)\mathbf{T}_u^{-1}=\mathbf{\Lambda}, \tag{37}$$

where α, β and γ satisfy $\alpha+\beta+\gamma=1$. $\mathbf{\Lambda}$ is a diagonal matrix. The transformation $\mathbf{T}_u$ is applied to $\mathbf{F}_1$, $\mathbf{F}_2$ and $\mathbf{F}_3$ to obtain the matrices $\mathbf{X}_d$, $\mathbf{Y}_d$ and $\mathbf{Z}_d$, respectively. The matched parameters (x',y',z') are extracted from the phases of elements at the main diagonals of $\mathbf{X}_d$, $\mathbf{Y}_d$ and $\mathbf{Z}_d$.

Clearly, the 3-D ESPRIT method does not need a matching step. After extracting the virtual far-field scattering centers described in (16), the second step is to transform the virtual ones into the real ones by using the functions (6) to (8).

4. Results

Some simulation results will be presented to demonstrate the performance of the near-field 3-D ESPRIT type method. Let us consider the backscattered data from a cubic object model with eight scattering centers at the corresponding vertices as shown in Fig. 4. The RCS of each scattering center is assumed to be 1 m^2.

Fig. 5(a) shows the estimated virtual positions of the scattering centers by the far-field 3-D ESPRIT algorithm at an SNR of 5 dB. Two hundred independent trials are displayed. The operating frequency range is $f=34.9$ GHz–35.1 GHz. And the distance R_0 is 4 m, clearly in the near-field zone of the object. The near-field estimated scattering centers are obtained by further exploiting (6) to (8), as shown in Fig. 5(b). Clearly, the near-field estimations are much closer to the real positions than the estimations of the conventional method without spherical wavefront curvature compensation.

To compare quantitatively the precision of the near-field compensation, we consider the root mean square error (RMSE) of the estimated positions such as

$$\mathrm{RMSE}=\sqrt{\frac{1}{3\cdot L}\sum_{l=1}^{L}(x_l-\widehat{x}_l)^2+(y_l-\widehat{y}_l)^2+(z_l-\widehat{z}_l)^2}\ \ (\mathrm{m}), \tag{38}$$

where (x_l,y_l,z_l) is the real position of the scattering center, $(\widehat{x}_l,\widehat{y}_l,\widehat{z}_l)$ is the corresponding estimated result, and L is the

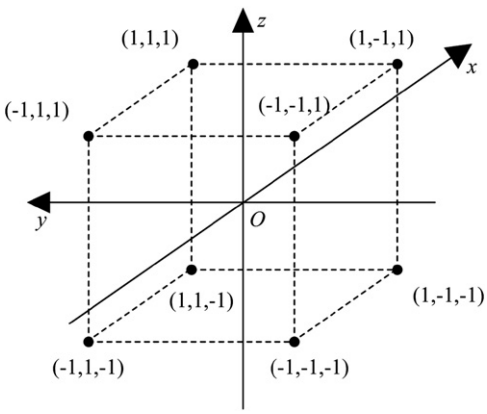

Fig. 4. The cubic object model with eight scattering centers.

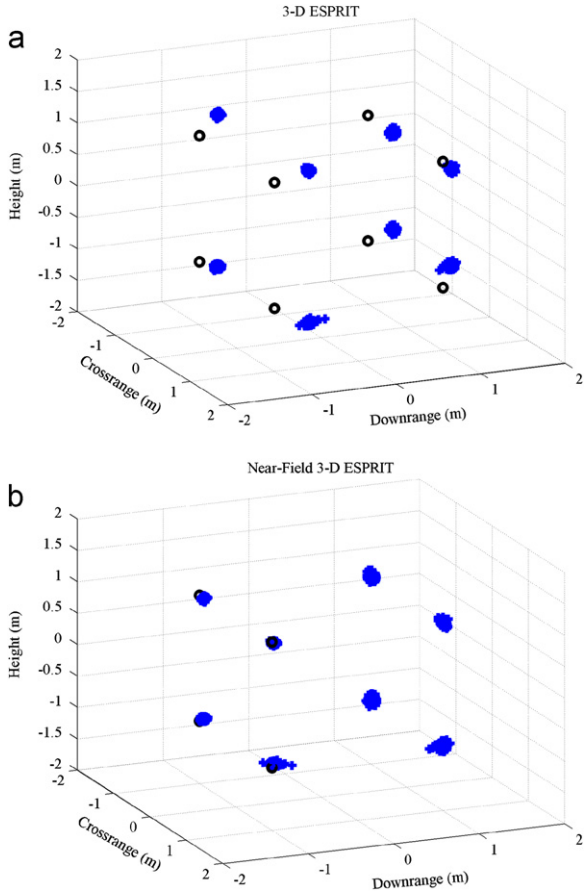

Fig. 5. Two hundred independent estimates of the positions of the scattering centers at SNR=5 dB and R_0=4 m, where "o" represents the real position, and the "+" represents the estimated result. (a) without near-field compensation, (b) with near-field compensation.

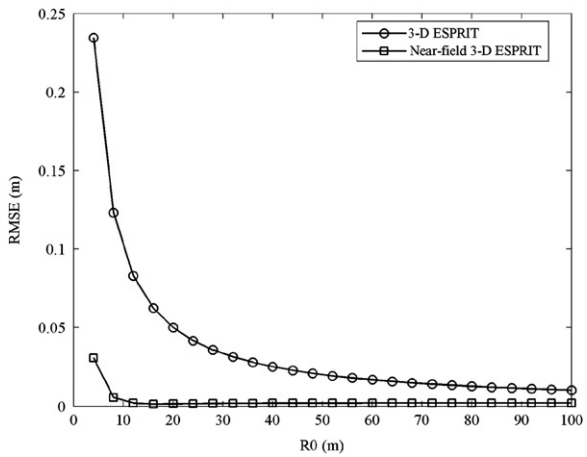

Fig. 6. RMSE characteristics of the 3-D ESPRIT method with and without the near-field compensation, as a function of the measuring distance R_0.

number of scattering centers. Fig. 6 shows the RMSE characteristics as a function of the measuring distance R_0 in the noiseless case. Clearly, the precision of the near-field 3-D ESPRIT method is much higher than the method

without near-field compensation, especially in the very near zone of the object.

5. Conclusions

We have presented a method for estimating the near-field 3-D scattering centers. For electrically large objects, the waves illuminating the object zone must be considered as spherical waves. The conventional methods based on the far-field assumption cannot be directly applied to the near-field scenario. We first formulated the near field compensation relations, and then presented a 3-D ESPRIT type algorithm. Combined with the compensation, the 3-D ESPRIT algorithm is capable of estimating the scattering centers of an object under spherical wave illumination. Simulation results show that a remarkable improvement in the near-field compensation can be achieved by the proposed method. The experimental verification of the near-field 3-D ESPRIT algorithm will be dealt with in the forthcoming work.

References

[1] E.F. Knott, Radar Cross Section Measurements, SciTech Publishing Inc., 2006.
[2] Z.M. Wang, W.W. Wang, Fast and adaptive method for SAR super-resolution imaging based on point scattering model and optimal basis selection, IEEE Transactions on Image Processing 18 (7) (2009) 1477–1486.
[3] K.T. Kim, H.T. Kim, Two-dimensional scattering center extraction based on multiple elastic modules network, IEEE Transactions on Antennas and Propagation 51 (4) (2003) 848–861.
[4] J.I. Park, K.T. Kim, A comparative study on ISAR imaging algorithms for radar target identification, Progress in Electromagnetics Research 108 (2010) 155–175.
[5] L.C. Potter, R.L. Moses, Attributed scattering centers for SAR ATR, IEEE Transactions on Image Processing 6 (1) (1997) 79–91.
[6] S.K. Han, H.T. Kim, S.H. Park, Efficient radar target recognition using a combination of range profile and time-frequency analysis, Progress in Electromagnetics Research 108 (2010) 131–140.
[7] L.C. Trintinalia, R. Bhalla, H. Ling, Scattering center parameterization of wide-angle backscattered data using adaptive Gaussian representation, IEEE Transactions on Antennas and Propagation 45 (11) (1997) 1664–1668.
[8] J. Zhou, H. Zhao, Z. Shi, Q. Fu, Analytic performance bounds on estimates of scattering center parameters, IEEE Transactions on Aerospace and Electronic Systems 43 (2) (2007) 813–826.
[9] D.L. Mensa, High Resolution Radar Cross-Section Imaging, Artech House, Boston, MA, 1991.
[10] R.O. Schmit, Multiple emitter location and signal parameter estimation, IEEE Transactions on Antennas and Propagation 34 (3) (1986) 276–280.
[11] C.E. Kassis, J. Picheral, C. Mokbel, Advantages of nonuniform arrays using root-MUSIC, Signal Processing 90 (2010) 689–695.
[12] R. Roy, T. Kailath, ESPRIT — Estimation of signal parameters via rotational invariance techniques, IEEE Transactions on Acoustics Speech and Signal Processing 37 (7) (1986) 984–995.
[13] A.B. Gershman, M. Rubsamen, M. Pesavento, One- and two-dimensional direction-of-arrival estimation: an overview of search-free techniques, Signal Processing 90 (2010) 1338–1349.
[14] Y. Hua, Estimating two-dimensional frequencies by matrix enhancement and matrix pencil, IEEE Transactions on Signal Processing 40 (9) (1992) 2267–2280.
[15] M.W. Tu, I.J. Gupta, E.K. Walton, Application of maximum likelihood estimation to radar imaging, IEEE Transactions on Antennas and Propagation 45 (1) (1997) 20–27.
[16] Y.D. Huang, M. Barkat, Near-field multiple sources localization by passive sensor array, IEEE Transactions on Antennas and Propagation 39 (7) (1991) 968–975.
[17] N. Yuen, B. Friedlander, Performance analysis of higher order ESPRIT for localization of near-field sources, IEEE Transactions on Signal Processing 46 (3) (1998) 709–719.
[18] C.A. Balanis, Antenna Theory: Analysis and Design, Wiley, New York, 2005.
[19] C.J. Bradley, P.J. Collins, D.G. Falconer, J. Fortuny, A.J. Terzuoli Jr., Evaluation of a near-field monostatic-to-bistatic equivalence theorem, IEEE Transactions on Geoscience and Remote Sensing 46 (2) (2008) 449–457.
[20] A. Jeffrey, Advanced Engineering Mathematics, Harcourt/Academic Press, Burlington, MA, 2002.
[21] S. Rouquette, M. Najim, Estimation of frequencies and damping factors by two-dimensional ESPRIT type methods, IEEE Transactions on Signal Processing 49 (1) (2001) 237–245.
[22] M. Cheney, B. Borden, Problems in synthetic-aperture radar imaging, Inverse Problems 25 (2009). ID: 123005 (18pp).
[23] Y.X. Wang, H. Ling, A frequency-aspect extrapolation algorithm for ISAR image simulation based on two-dimensional ESPRIT, IEEE Transactions on Geoscience and Remote Sensing 38 (4) (2000) 1743–1748.
[24] W. Zhi, M.Y.-W. Chia, Near-field source localization via symmetric subarrays, IEEE Signal Processing Letters 14 (6) (2007) 409–412.
[25] J. Liang, D. Liu, Passive localization of mixed near-field and far-field sources using two-stage MUSIC algorithm, IEEE Transactions on Signal Processing 58 (1) (2010) 108–120.